AIAA 2003-5105
A 3-D CFD Analysis of the Space Shuttle RSRM With Propellant Fins @ 1s Burn-Back

R. A. Morstadt
ATK Thiokol Propulsion Corp.,
A Division of ATK Aerospace Co.
Brigham City, UT

39th Joint Propulsion Conference & Exhibit
20-23 July 2003
Huntsville, Alabama

A 3-D CFD Analysis of the Space Shuttle RSRM with Propellant Fins @ 1s Burn-back

R. A. Morstadt*
ATK Thiokol Propulsion Corp., a Division of ATK Aerospace Company
Brigham City, UT

Abstract

In this study 3-D Computational Fluid Dynamic (CFD) runs have been made for the Space Shuttle RSRM using 2 different grids and 4 different turbulent models, which were the Standard KE, the RNG KE, the Realizable KE, and the Reynolds stress model. The RSRM forward segment consists of 11 fins. By taking advantage of the forward fin symmetry only half of one fin along the axis had to be used in making the grid. This meant that the 3-D model consisted of a pie slice that encompassed 1/22nd of the motor circumference and went along the axis of the entire motor. The 3-D flow patterns in the forward fin region are of particular interest. Close inspection of these flow patterns indicate that 2 counter-rotating axial vortices emerge from each submerged solid propellant fin. Thus, the 3-D CFD analysis allows insight into complicated internal motor flow patterns that are not available from the simpler 2-D axi-symmetric studies. In addition, a comparison is made between the 3-D bore pressure drop and the 2-D axi-symmetric pressure drop.

Introduction

Reliable predictions of the flow-field in the RSRM are required to provide boundary conditions such as heat transfer coefficients and pressure loads for component designers. These predictions have evolved from initial 1-D results using ballistics code predictions, to 2-D axi-symmetric analyses (see Laubacher[1], Eaton, et al.[2], and Ahmad, et al.[3]), to simulations with a full 3-D geometry. A 3-D analysis is desirable from the standpoint of modeling the RSRM fin geometry. The drawback is that the analysis is computationally intensive, because of the large motor size and the corresponding large number of grid cells.

The 3-D nature of the RSRM grain design is only present in the forward motor segment. The forward motor segment consists of 11 fins as shown in Fig. 1 and Fig. 2. By taking advantage of the forward fin symmetry only half of one fin along the axis was needed to make the grid. This meant that the 3-D model consisted of a pie slice that encompassed 1/22nd of the motor circumference and went along the axis of the entire motor.

Discussion

Two grids were available for this study, i.e., a Gambit® grid and an ICEM® grid. The preprocessor Gambit® code was used to generate a grid that consisted mostly of tetrahedral cells (503, 497 cells) using the boundary layer option in the nozzle, which provided a better control of y+ for the nozzle wall cells. The second grid consisting mostly of hexahedrons or bricks (879,481 cells) was generated using the grid code ICEM®. At first it was thought that the hexahedron model would have a better solution. The general thinking being that rectangular-shaped cells or bricks would provide a better solution. However, the results for this particular study indicate that the better y+ value in the walls cells of the tetrahedral grid outweighed any benefit from the hexagonal grid.

The single-phase flow option was used in Fluent® assuming a homogeneous perfect gas. The gas thermal conductivity and molecular viscosity were specified as temperature dependent. Mass addition at the propellant surface was calculated using the burning rate power law and the gas was injected into the motor at the adiabatic flame temperature. A nozzle wall temperature varying in the axial direction was specified along the nozzle boundary. Internal insulation parts were specified with a constant wall temperature. Heat conduction in the gas and to the walls was included.

The 4 different turbulent models used in this study were the Standard KE, the RNG KE, the Realizable KE, and the Reynolds stress model. The first 3 turbulent models are two-equation models, i.e., one transport equation for the turbulent kinetic energy and one transport equation for the turbulent dissipation. The Reynolds

---

*Sr. Principal Engineer, Sr. member AIAA

stress model includes a transport equation for each turbulent stress component.

In this study the initial Fluent® run was usually made with the RNG turbulence model, because this model was found to be the most stable. The RNG model was used along with the boundary condition that the turbulent viscosity ratio is set equal to 100 on the propellant surface. The turbulent viscosity ratio limit was set high everywhere else. After convergence (about 2200 to 3000 iterations) was assured the propellant surface boundary condition was changed to the intensity and hydraulic diameter option. Subsequent iterations were run to lower the limit on the turbulent viscosity ratio. Almost all the runs in this study had a final turbulent viscosity ratio upper limit set equal to 10,000 for the entire flow field

One case in Table 1 for the Gambit® grid was run with a turbulent viscosity ratio equal to 100 on the mass inlet boundary and had no corresponding upper limit for the viscosity ratio. The Fluent® user guide section stated that for fully developed turbulent flow the turbulent viscosity is roughly two orders of magnitude larger than the molecular viscosity. This statement supports this choice for the B.C. on the mass inlet for the viscosity ratio equal to 100. For the other B.C. option using the hydraulic diameter, the Fluent® user guide stated that the hydraulic diameter is multiplied by a 0.07 factor. Using this result the other standard formulae yields a turbulent viscosity ratio equal to 240. (These procedures are consistent with a jet. In contrast the viscous B.C. in pipe flow without mass addition has a turbulent viscosity ratio equal to 0.) Although, the 100-viscosity ratio on the mass inlet boundary has the advantage of not requiring an upper limit, the 3D pressure prediction is not as good as the 10,000 upper limit as shown in Table 1.

Results

A summary of all the significant RSRM 3-D Fluent® runs is presented in Table 1. The 2 best runs were found using the Gambit® grid and the RNG turbulence model. The first order RNG run had a head-end pressure of 921.9 psia with a bore pressure drop of 178.5 psi. The corresponding RNG using the power law for the higher order solution had a head-end pressure of 943.8 psia with a bore pressure drop of 192.3 psi.

A graphical comparison of these results with the pressure distribution down the bore with the QM-7 and FSM-9 static test motor test data along with the 2-D axi-symmetric case is shown in Fig. 3. Close inspection of Fig. 3 indicates that the 3-D prediction has about the same bore pressure distribution as the 2-D axi-symmetric prediction, but attributes more of the pressure drop as coming from the fin region. Part of this difference can be attributed to the presence of 3-D flow patterns. Typically, Fluent® has tended to over-predict RSRM bore pressure drops, especially, for the 1s burn-back. The 2-D pressure drop shown in Fig. 3 per Ahmad, et al.[3] with turbulent model adjustments made a good comparison with the QM-7 test data. Several explanations have been offered for the large 3-D fin bore pressure drop. One possible explanation is that the turbulent model needs to be adjusted. Another explanation is that the geometry of the model should be changed to reflect that fact that the fins have burned back slightly after 1 second, opening the flow area, and thereby reducing the pressure drop.

An indication of these 3-D flow patterns is illustrated in Fig. 4 and Fig. 5. Shown in Fig. 4 is one RSRM fin looking from the aft end toward the front of the forward segment. The black lines that are shown mark the symmetry planes for the one-half fin analyzed by Fluent®. In the Fluent® post-processor one-half of the fin is mirrored on the other side to present the one whole fin to the viewer. Note that the bore centerline is actually at the bottom of these figures and the main CP bore diameter, which is at the aft end of the forward segment, is represented by the slightly curved surface closest to the viewer. The large forward fin protruding upward is actually the hollow cavity of the submerged fin. In this view it is above the main CP bore diameter. On the lower left-hand side the viewer can discern the edge of the solid propellant fin that protrudes into the main CP bore. The small cavity in front of the large fin is the transition region.

The path lines shown in Fig. 4 are actually viewed looking into the 3-D motor interior cavity formed by the symmetry planes and the propellant surfaces. On the other hand the oil path lines presented in Fig. 5 are actually on the propellant surfaces. This presentation is similar to the idea of oil smears that are sometimes used for flow visualization in cold flow experimental tests.

Close inspection of Fig. 4 and Fig. 5 indicates that a vortical or swirling flow appears downstream on either side of the solid propellant fin that protrudes into the

main CP bore. One would expect that the fins with their large surface area could be a strong source for rotational flow. Actually, the forward fins are the strongest source for axial vorticity in the whole motor. Recall from the Culick[4] analytical solution that mass injection from propellant surfaces is a source for vorticity. This process can be visualized as shown in Fig.2. Recall Stoke's theorem in the following form for the vorticity:

$$\zeta_n = (\nabla \times \vec{v})_n = \lim_{A \to 0} \frac{1}{A} \oint \vec{v} \cdot d\vec{l}$$

where the vorticity is normal to the surface that contains the line integral. From this definition one can imagine planes in the fins that contain the velocity profile that are perpendicular to the motor axis as shown by the actual vector plot in Fig. 6. This means that the vorticity inside the fins is in the axial direction. Also, recall via the inviscid Culick solution that vorticity can be created by mass injection alone. Furthermore, for incompressible flow without turbulence, the transport of vorticity can be written as follows:

$$\frac{D\vec{\zeta}}{Dt} = \nu \nabla^2 \vec{\zeta}$$

If the viscous diffusion is small, the vorticity will remain predominantly in the same direction when it transported out of the fins. If one were to apply the rectangular integral path shown in Fig. 2 to the centerline of the slot, they would find that the vorticity there is zero and, in fact, the vorticity on the other side would have the opposite direction. Conceivably, then, one could expect 2 vortices emerging from the submerged slot rotating in opposite directions. Close inspection of the flow patterns in Fig. 4 and Fig. 5 indicate that there are 2 vortical flow patterns emerging from one fin slot. This is confirmed by Fig. 7, which shows the plot of velocity vectors in the plane perpendicular to the axis about 0.7 m. downstream of the fin termination. In fact, as shown the vortices are counter-rotating. As the flow accelerates rapidly into the bore from the confined volume of the submerged fins, the strongest vortices appear next to the propellant surface. However, further inspection of Fig. 7 shows some weaker re-circulation closer to the centerline. Part of this motion can be attributed to the mass injection from the propellant fins that protrude into the main bore. Vortex pairs for aft fins have also been predicted by CFD per Chaouat[5].

Classical hydrodynamic solutions are available for idealized line vortices in 2-D planar flow per Lamb[6], Milne-Thomson[7], and Robertson[8]. In 2-D planar geometry a vortex pair with the spin shown in Fig. 7 will move away from the wall. This motion is not apparent in this solution, but this is not surprising, because the pie-slice geometry is more restrictive with the volume of space moving toward the centerline than the simpler 2-D planar geometry. In addition viscous effects are very dissipative going down the bore as shown by Fig. 8 for a cross-section 1.6 m. upstream of the forward joint. The vortex motion has dissipated enough at this location that the mass injection velocity is visible.

When one applies the same geometrical arguments to the CP bore or the slots, it is found that those locations produce only circumferential vorticity. This observation is corroborated by a plot of vorticity on the propellant surface as a function of axial distance as shown in Fig. 9. Note that the 2-D representation of the forward fins predicts almost no vorticity in comparison to the 3-D RSRM run, but there is circumferential directed vorticity generated in the slots. The scatter in this 3-D vorticity plot is due to representation or projection of the circumferential distribution of the vorticity onto the 1-D axial coordinate.

The Mach number distribution next to the symmetry planes and the propellant surfaces is shown in Fig. 10 Close inspection of this plot on the lower left-hand symmetry plane shows that the Mach number is the highest where the flow comes off the solid propellant fin tip into the aft-end main CP bore region. In contrast the Mach number is low in the space between the solid fins where they meet the main CP bore just downstream of the transition region. This low speed region coincides with the region between the two vortical flows shown in Fig. 4 and Fig. 5.

As shown in Fig. 11 the static pressure distribution in one 3-D fin varies considerably across the propellant surface. This is in contrast to the single value for the static pressure given on the motor centerline as typified by the axial pressure distributions shown in Fig. 3. Notice that there are two small low-pressure spots just downstream of the transition region. These locations correspond to the vortical flows shown in Fig. 4 and Fig. 5.

Summary and Conclusions

In the past results from 2-D simulations have been used to provide pressure loads for grain-structural analysts. With some manipulation the 2-D pressure distribution in the fin area was projected onto the structural model. This process can now be repeated in a more direct manner using the Fluent® 3-D pressure distribution.

In this study the RNG turbulence model was the most effective for producing a reasonable converged solution. The 2 best runs are using the Gambit® grid and the RNG turbulence model. The RSM turbulence model was not stable enough for this 3D geometry, although it provided very good predictions for 2-D axi-symmetric predictions.

The bore pressure drop and distribution is not only affected by the turbulence models and their parameters, but can be affected by other things including 3-D geometry. This study indicates that 3-D effects in the forward fins will affect the pressure distribution in that region and the flow pattern emerging from the fins.

Close inspection of Fig. 3 indicates that the 3-D prediction has about the same axial pressure distribution as the 2-D axi-symmetric prediction, but attributes more of the pressure drop as coming from the fin region.

Acknowledgements

The author would like to thank Brian Laubacher for his help and special effort on setting up this problem. The author would also like to acknowledge Thomas Scheidegger at Fluent® for his timely advice on running Fluent®.

References

[1]Laubacher, Brian A., "Internal Flow Analysis of Large L/D Solid Rocket Motors", 36th AIAA Joint Propulsion Conference, AIAA paper no. 2000-3803, July 16-19, 2000.

[2]Eaton, A. M., and Laubacher, B. A., "Simulation of the Reusable Solid Rocket Motor Flow Field Near Ignition", 38th JANNAF Combustion Subcommittee, Destin, Florida, April, 2002.

[3]Ahmad, R.A., Morstadt, R.A., Eaton, A.M., "RSRM and ETM-03 Internal Flow Simulations and Comparisons", 39th AIAA Joint Propulsion Conference, AIAA paper no. 2003-5105, July 20-23, 2003.

[4]Culick, F.E.C., "Rotational Axi-symmetric Mean Flow and Damping of Acoustic Waves in Solid Propellant Motors", AIAA Journal, vol. 4, No.8, pp. 1462-1464, 1966.

[5]Chaouat, Bruno, "Flow Analysis of a Solid Propellant Rocket Motor with Aft Fins", Journal of Propulsion and Power, Vol.13, No. 2, pp. 194-196, March-April 1997.

[6]Lamb, H., Hydrodynamics, 6th Ed., pp. 223-224, Dover Publications, N.Y., 1945.

[7]Milne-Thomson, L. M., Theoretical Hydrodynamics, 4th Ed., p. 361, MacMillian & Co., N.Y., 1960.

[8]Robertson, J.M., Hydrodynamics in Theory and Application, p. 133, Prentice-Hall, Inc., Englewood Cliffs, N.J., 1965.

Table 1. Summary of RSRM 3-D Fluent® Runs with Fins @ 1s Burn-back

Grid	Turb. Model	Turb. Viscosity Ratio Limit	Convergence	Order of Solution	Head-end Press. (psia)	Bore Delta Press. (psi)	Wall Cell Y+
Gambit®	Standard	10,000	Fair: Energy relax. values slightly less than default	Power Law	1054.3	298.4	Nozzle 25-235 Slot < 830
Gambit®	RNG	10,000	Very Good	1st	921.9	178.5	Nozzle 25-230 Slot < 604
Gambit®	RNG	10,000	Good: Energy & mom. relax. values slightly less than default	Power Law	943.8	192.3	Nozzle 25-235 Slot < 607
Gambit®	RNG	100 @ mass inlet	Good: Energy relax. slightly less than default	Power Law	952.3	204.3	Nozzle 20-230 Slot< 640
Gambit®	Realiz-able	10,000	Good	Power Law	1031	284	Nozzle 25-230 slot < 685
Gambit®	RSM	10,000	Fair: Energy relax. slightly less than default & some high residuals	Power Law	1015	227.1	Nozzle 25-270 slot < 680
ICEM®	Standard	10,000	Good	1st	935.5	319.9	Nozzle<1,800 Slot<980
ICEM®	Standard	10,000	Fair: Large fluctuations in K & epsilon	Power Law; 1st Order for K-E	960.6	319.7	Nozzle <1,800 slot < 1,000
ICEM®	Realiz-able	10,000	Poor: Relaxation values less than default; bad nozzle centerline values	2nd	996.3	302.4	Nozzle< 2,100 Slot < 1,700
ICEM®	RNG	10,000	Good	1st	878	265	Nozzle <1,650 slot < 640
ICEM®	RNG	10,000	Good	Power Law	907.4	256.8	Nozzle <1,850 slot < 680
ICEM®	RNG	100,000	Good	Power Law	1061.1	411	Nozzle <2,100 slot < 1,050
ICEM®	RSM	10,000	Fair: Relax. values less than default	1st	857.1	182.5	Nozzle <2,200 slot < 980

1) ICEM® grid has 879,481 cells that are mostly bricks (hexahedrons). Heat transfer on walls & nozzle
2) Gambit® grid has 503,497 cells that are mostly tetrahedrons. Heat transfer on walls & nozzle
3) All turbulence models used wall functions. The Realizable model used the non-equilibrium wall function.

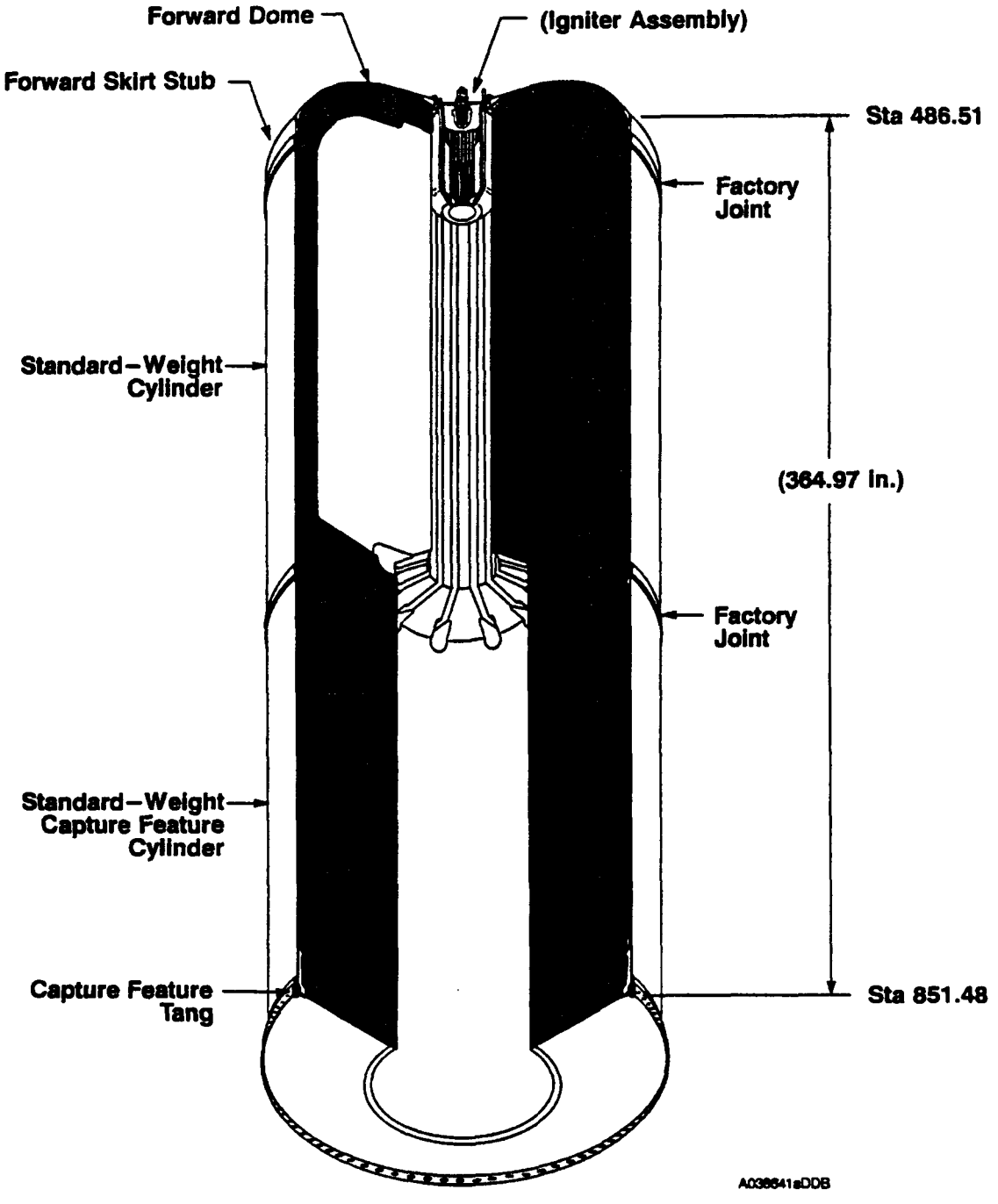

Figure 1. RSRM Forward Segment showing Propellant Fins

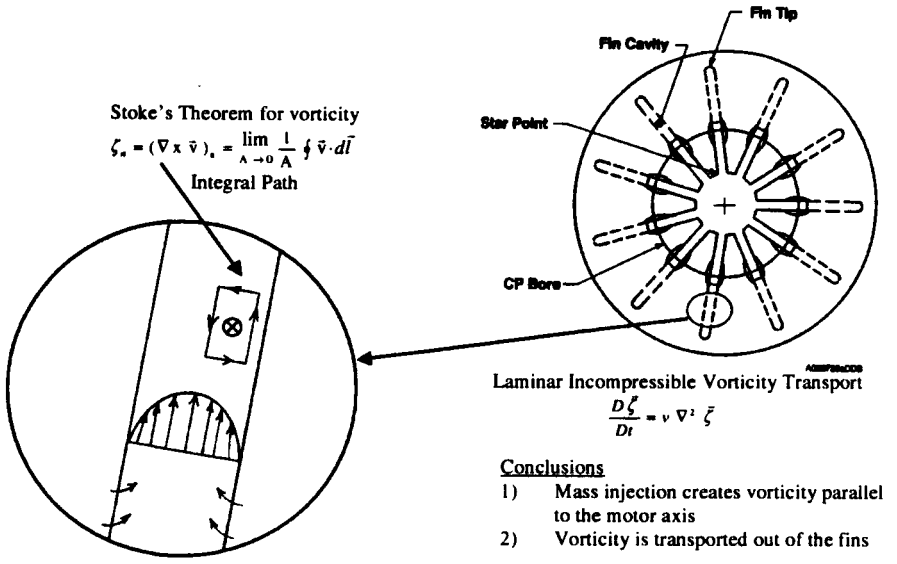

Figure 2. Axial Vorticity is Created in Fins and Transported Downstream

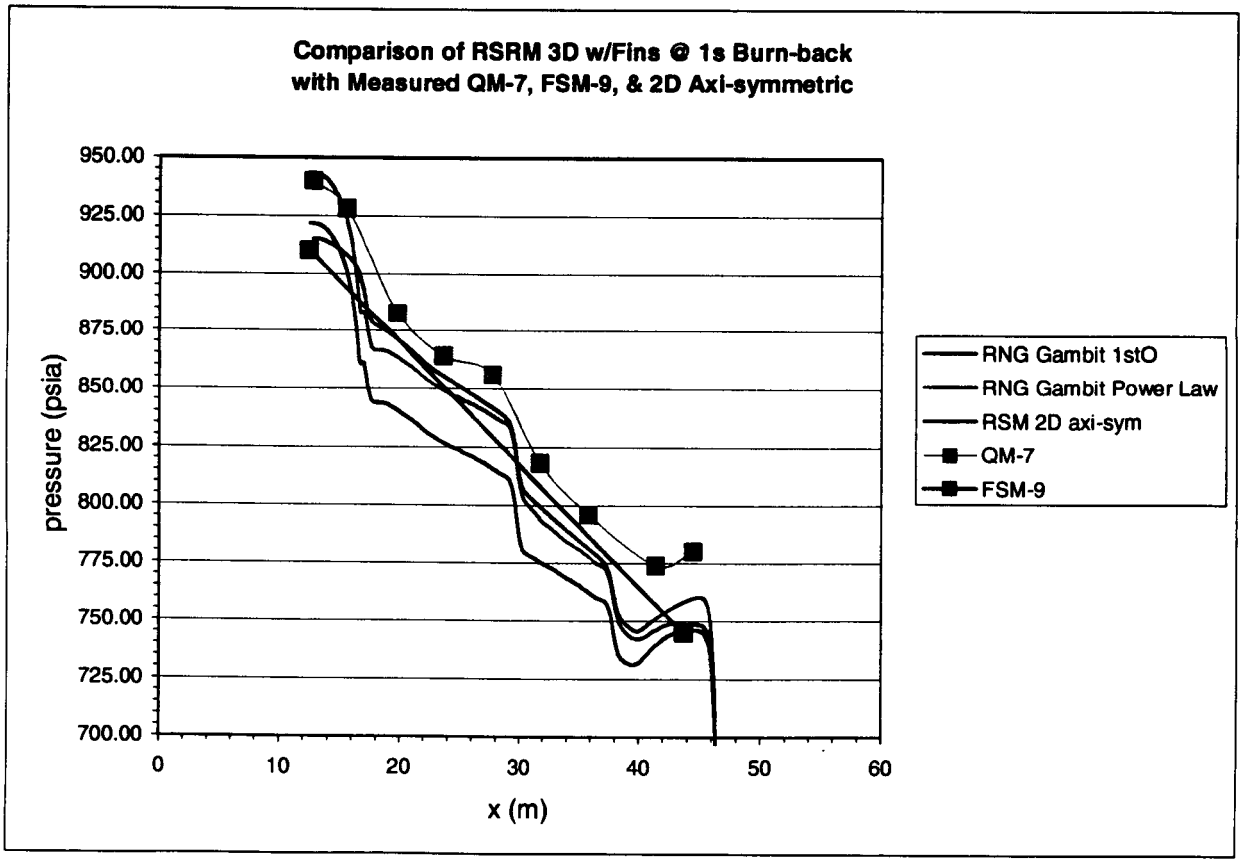

Figure 3. RSRM Bore Pressure Distribution

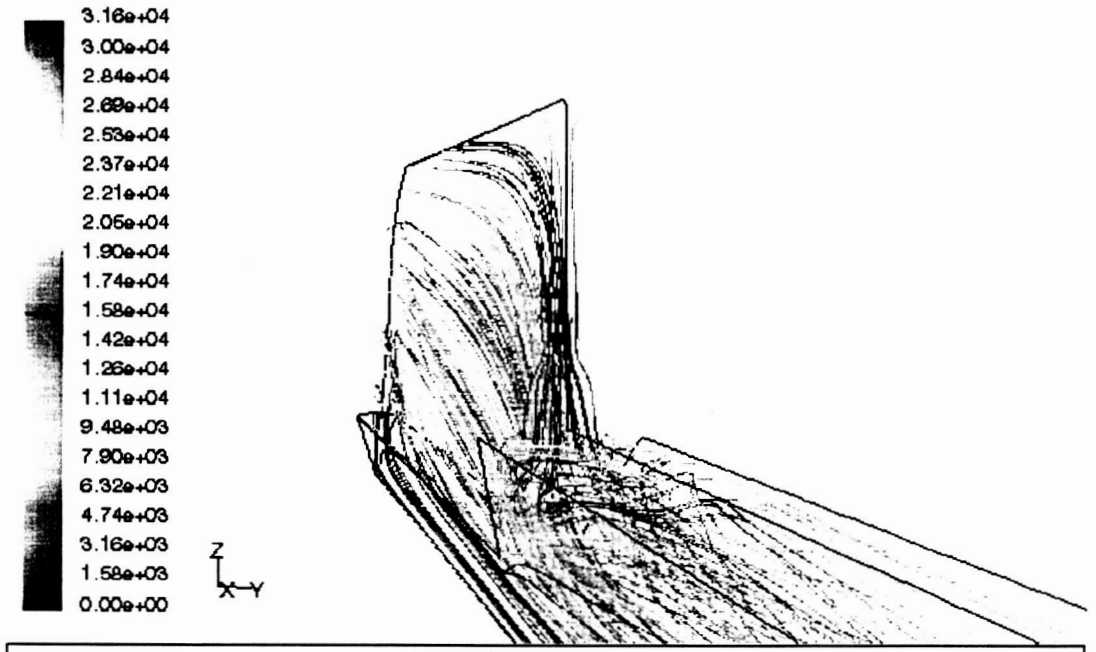

Figure 4. Path lines shown inside the volume of one submerged RSRM 3-D fin slot

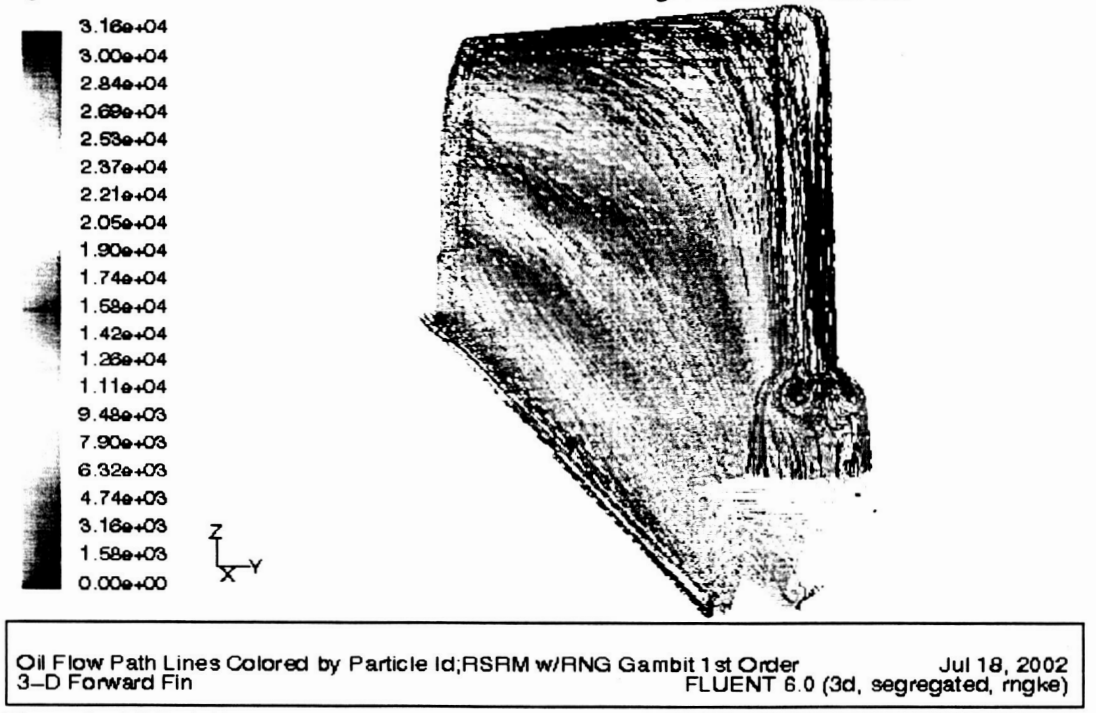

Figure 5. Oil Path lines on one submerged RSRM 3-D fin slot surface.

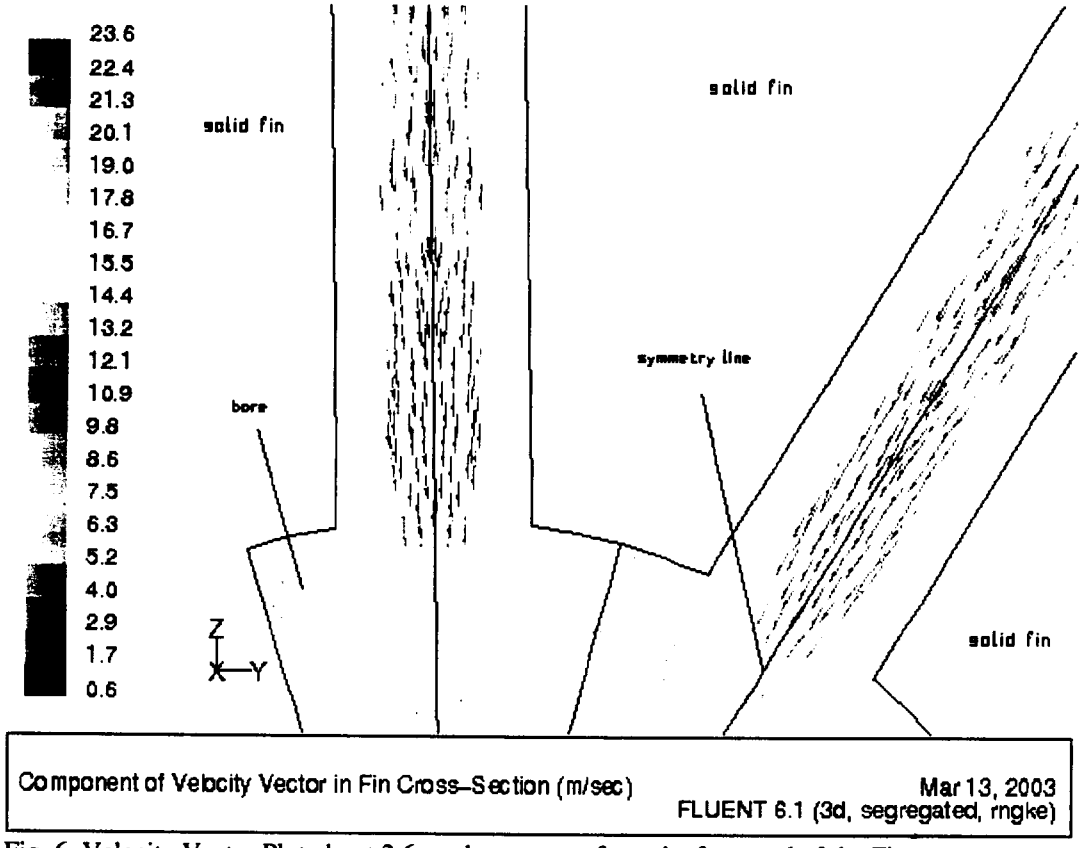

Fig. 6. Velocity Vector Plot about 2.6 m. downstream from the front end of the Fin.

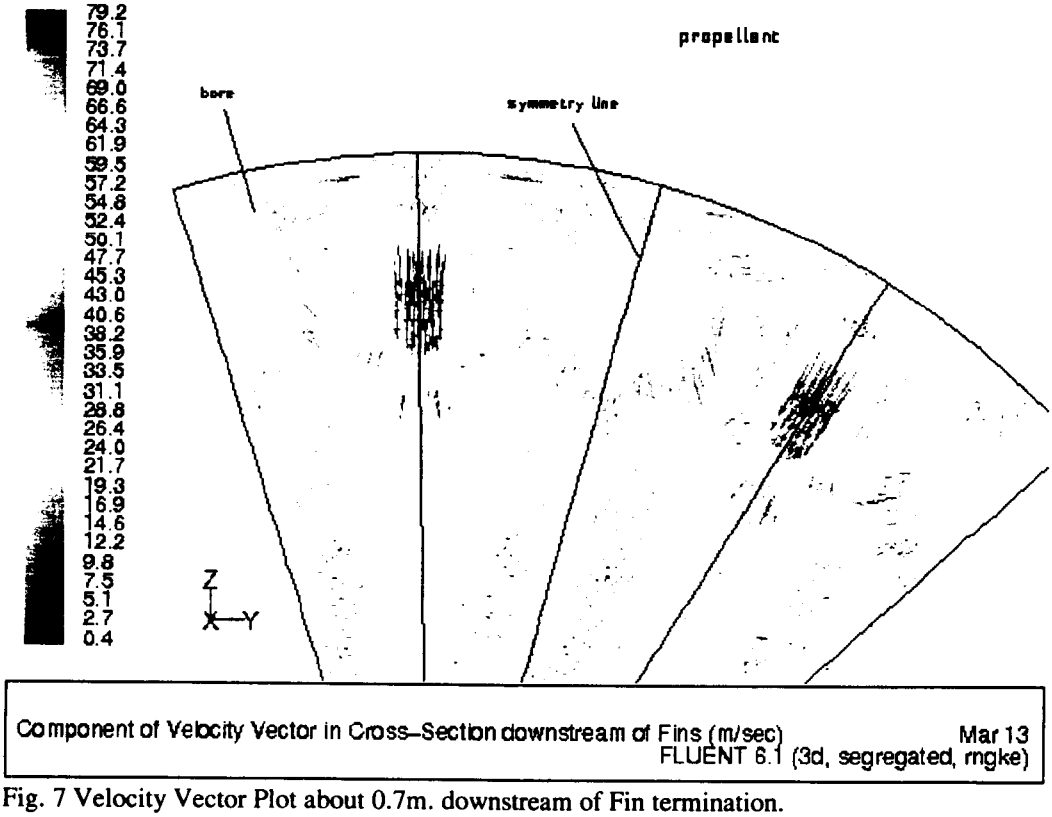

Fig. 7 Velocity Vector Plot about 0.7m. downstream of Fin termination.

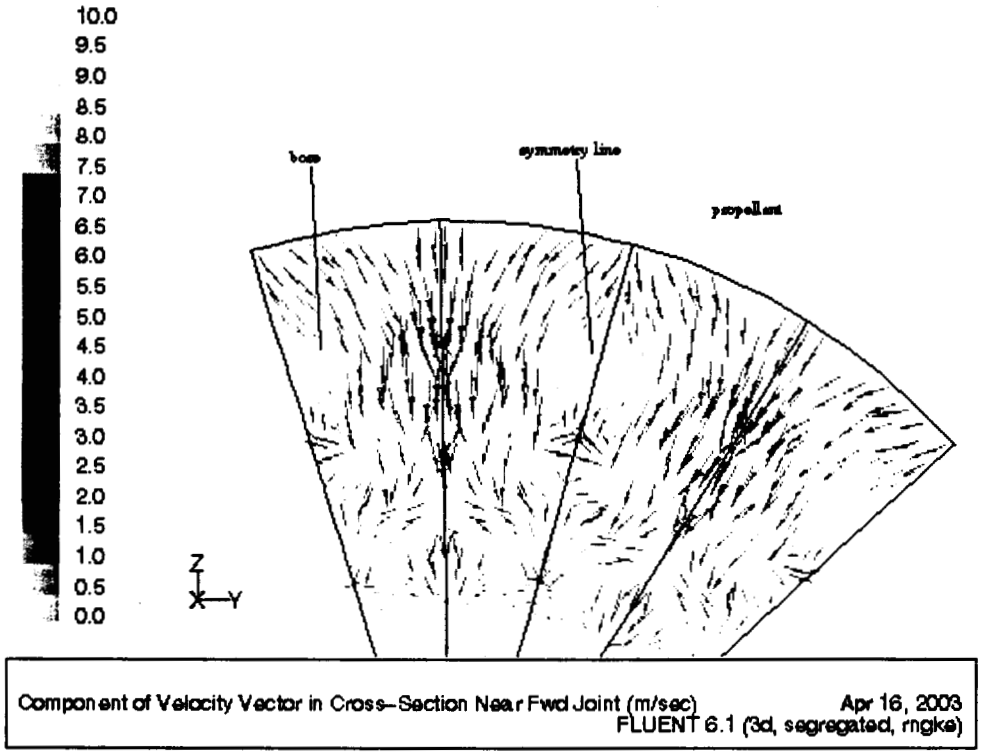

Figure 8. Velocity Vector Plot about 1.6 m. upstream of the Forward Field Joint.

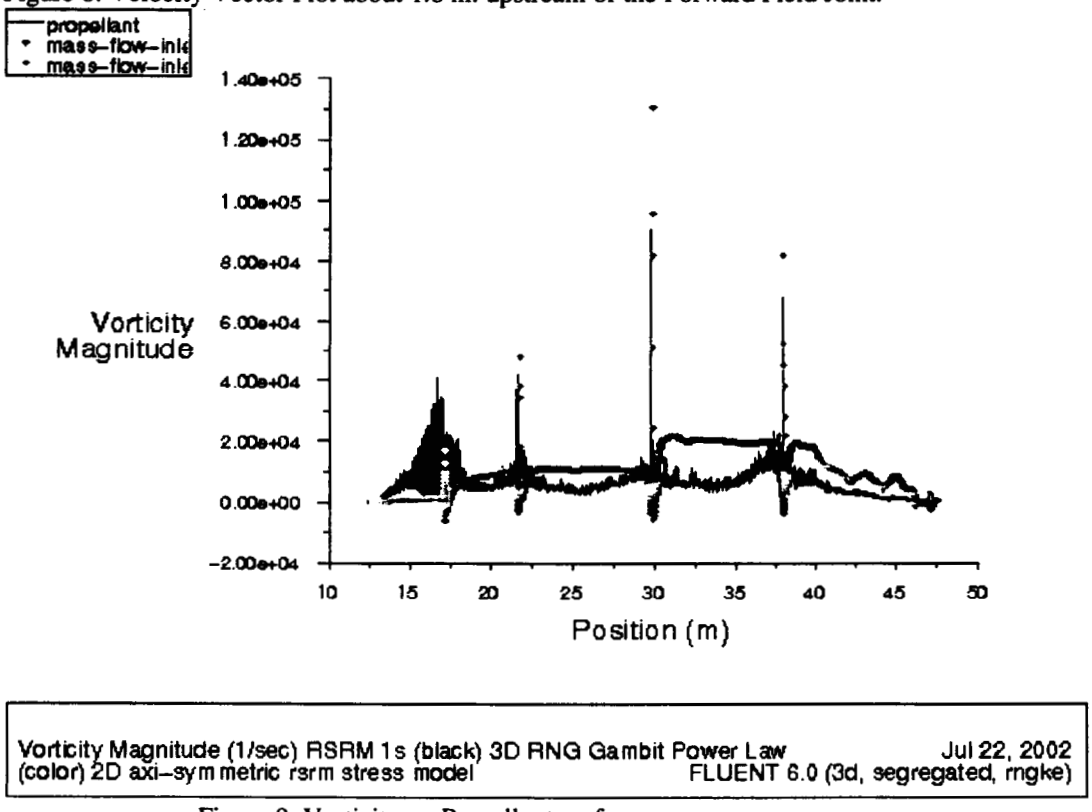

Figure 9. Vorticity on Propellant surface

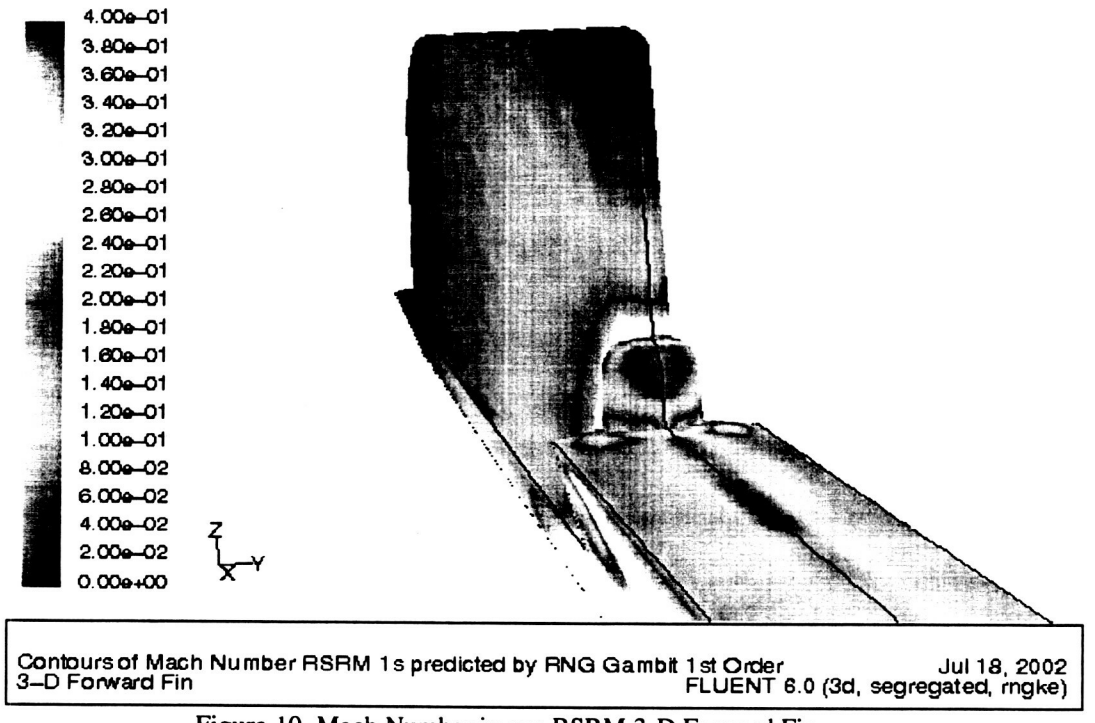

Figure 10. Mach Number in one RSRM 3-D Forward Fin

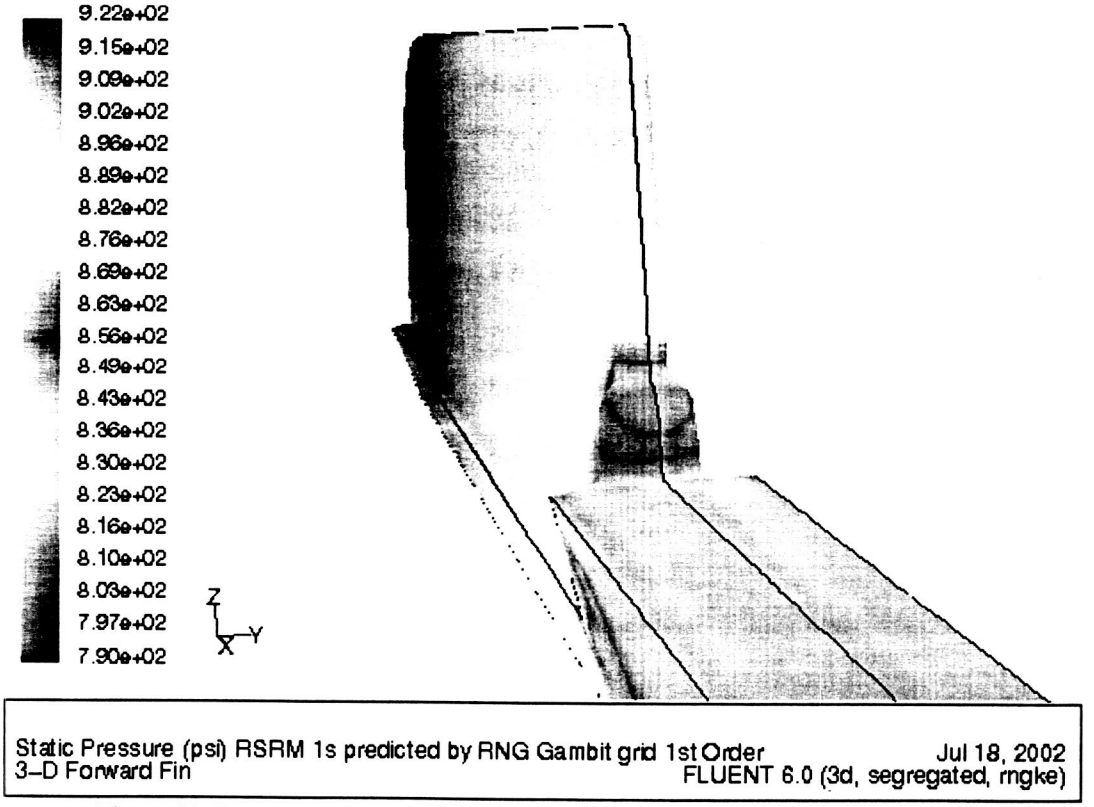

Figure 11 Pressure Distribution in one RSRM 3-D Forward Fin